Image-based investigation into the primary fabric of stress transmitting particles in sand

Fonseca, J.*[1], Nadimi, S. [1], Reyes-Aldasoro, C.C[1], O'Sullivan, C.[2], Coop, M.R.[3]

Abstract

This paper uses three dimensional images of a natural silica sand to analyse the mechanisms of stress transmission under triaxial compression. As discussed in Fonseca et al. (2012) the irregular morphology and the locked fabric that can be found in natural sands lead to the formation of contacts with extended surface areas. Most of our current understanding on the stress transmission phenomena comes, however, from DEM simulations and photoelastic experiments using idealised grain shapes and contact topologies. Direct measurement of stress transmission in assemblies of real soil grains is a challenging task. The present study postulates that important insight can be obtained from following the evolution of the intergranular contacts as the grains rearrange and considers how these rearrangements enhance the stability of the material. The methodology consists of measuring the geometrical data of the individual grains and their associated contacts obtained at successive load stages in the post-peak regime (after shear band formation). Statistical analysis of the vectors normal to the contacts reveals a realignment of these vectors in the direction of the major principal stress; this is a clear indication of the formation of force chains. Subsequent analysis showed that these columnar structures of stress transmitting grains were associated with larger contact surfaces and have distinct patterns in the region affected by the formation of the shear band. An algorithm based on a stability and load transmission criteria was developed to contribute new insight into the characterisation of the load-bearing sand particles.

Key words: fabric/structure of soils; 3D microscopy; shearing; locked sand; stress-transmission
IGS: D01, D03, D06

1. City, University of London, UK
2. Imperial College London, UK
3. University College London, UK (formerly City University of Hong Kong, H-K)

*Corresponding author

INTRODUCTION

Inter-particle stress transmission is a key factor that determines the mechanical behaviour of granular materials, including soil. Recent decades have witnessed significant advances on our understanding of the physical principles that underpin stress transmission phenomena. Photo-elastic experiments and discrete element method simulations have provided evidence that stress transmission in granular materials takes place through well-defined paths termed force chains (Ostojic et al., 2006; Silbert et al., 2002; Tordesillas et al., 2010; Zuriguel et al., 2007; Radjai et al. 1998). Force chains are columnar-like structures formed by the particles that carry the majority of the load in the system (Majmudar and Behringer, 2005; Lin and Tordesillas, 2014). This subset of particles often defined as those carrying above average contact forces is referred to as the strong network. Surrounding the force chains are the particles in the complementary weak network, the subset of contacts not in the strong network, which serve to provide the chains the necessary support (Tordesillas and Muthuswamy, 2009; Barreto and O'Sullivan, 2012). Under continued loading and loss of lateral support due to dilatation, these axially compressed particle columns that are the strong network become unstable and prone to buckling and this has been related to the formation of shear bands (Oda and Kazama, 1998; Rechenmacher et al 2010; Tordesillas et al., 2012). Clear experimental evidence of the formation of force chains in sandstone is provided by Fonseca et al (2013a); the rupture of the cement between grains during triaxial compression leads to the formation of vertical columns of horizontally unbonded grains, which in localised regions tend to collapse as shearing progresses.

Forces are transmitted only through the interparticle contacts; the non-uniformity of the size and orientation of these contacts as well as the variation in the properties of the particles forming the contacts, leads to strong inhomogeneities in the forces chains (Radjai et al. 1998). Under shear an anisotropic contact network develops because new contacts are formed along the major principal stress while some are lost perpendicular to it, this was observed in experiments with sands (Oda, 1972; Fonseca et al., 2013b) and DEM simulations (Rothenburg and Bathurst 1989; Thornton 2000). Radjai et al. (1998) showed that since the strong network continually aligns in the direction of the most compressive principal stress it is more anisotropic than the weak network.

Tordesillas et al. (2010) introduced the concept of force cycles to characterise the mutually supportive structures, analogous to structural trusses, that emerge during granular material deformation and which prevent failure. Tordesillas et al. observed that force chains tend to stabilise under a 3-cycle contact triangle topologies (triangular trusses) with neighbouring grains. These 3-cycle contacts are more effective than other contact topologies in providing resistance to loading by inhibiting relative particle rotations and providing strong lateral support to force chains (e.g., Tordesillas et al., 2011). The three-force cycles act to support the load and secure the stability of the force chain columns. Loss of contacts and rupture of 3-cycles leads to force chain failure by buckling.

Characterisation of force chains is commonly achieved by discriminating between forces of different magnitudes (Ostojic et al., 2006). Force chains can be visually identified by representing contact forces aslines whose thickness and/or colour indicates magnitude (Voivret et al 2009; Radjai et al., 1998). The complexity and non-linearity of the force chains in 3D has been shown by identifying the paths of maximum contact force (Makse et al., 2000). Peters et al. (2005) characterised force chains in an assembly of disks based on principles of quasi-linearity and stress concentration. Zuriguel et al. (2007) used least squares estimation to fit straight lines to chains identified in photoelastic experiments; they observed a well-defined correlation between the orientation of the chains and the angular distribution of contacts. Zuriguel et al. also reported on different modes of stress transmission for the case of disks when compared with the sample of elliptic cylinders. The splitting and merging of the force chain paths through granular media was investigated by Bouchaud et al. (2001). Hanley et al. (2015) used a simple link-node model to show that the peak major principle stress these force chains can resist is directly proportional to the confining stress, in line with the Mohr-Coulomb failure criterion.

The current study makes use of x-ray micro computed tomography (micro-CT) coupled with three dimensional (3D) image analysis tools to investigate the network of stress transmission in specimens of real sand. This comprehensive study follows the preliminary work presented in Fonseca et al. (2014). Following the description of the material and the experimental methods, a statistical analysis of the orientation of the contact vectors comprising both the contact normal and branch vectors is presented. Then the spatial distribution of these vectors is investigated to provide insight into the networks of stress transmitting particles.

MATERIAL and METHODS

This section describes the sand used in the experiments as well as the sampling technique to obtain the intact specimens and the sample preparation technique of the reconstituted samples. The methodology employed here consisted of carrying out triaxial tests, impregnating the sample with resin to preserve the fabric at various stages of deformation, extracting small cores for imaging at different locations and finally analysing the 3D images in order to obtain the required information in terms of grains rearrangements and contacts evolution under loading. Only key aspects of are described here, Further details on the material and the experimental procedures can be found in Fonseca (2011).

Reigate sand

Reigate sand, the material used here, comes from a formation that is part of the Folkestone Beds (Lower Greensand) from Southeast England in the UK. In its intact state, Reigate sand is characterised by very high densities and a locked fabric and meets the “locked sand” criteria proposed by Dusseault and Morgensten (1979). This locked fabric enabled the use of block sampling and so effectively undisturbed samples were considered in this experimental study, as discussed in more detail in Fonseca (2011). In its intact state, Reigate sand is a quartz-rich sand with a median grain diameter of approximately 300μm (this value decreases for the samples prepared in the laboratory, as discussed in Fonseca et al., 2012). The particle morphology varies from near-spherical grains to highly non-spherical grains with embayments. Microstructural characteristics to note include the abundance of large flat and concavo-convex contacts, in most cases forming multiple contact regions. These features are evident in the optical microscope image of the intact sand presented in Figure 1. In addition, fissures within the solid grains are also commonly found in this geologically old, once deeply buried sand. These fissures tend to open up during reconstitution of the soil, which explains the different particle size distribution between the intact and the reconstituted sand (Fonseca et al., 2012).

Experiments

Triaxial compression tests were carried out on both intact and reconstituted samples, 38mm in diameter and 76mm high, of the sand at similar densities in a dry state, a comprehensive description of the tests can be found in Fonseca (2011). The intact triaxial samples were obtained by carefully trimming an initial block of soil. The samples' long axis orientations corresponded to the vertical in situ orientation. The reconstituted samples were created using sand taken from the trimmings of the intact samples. Each sample was isotropically compressed to 300kPa at a rate of 50kPa/hour and then subjected to strain controlled compressive shearing at a rate of 1%/hour. The specimens were observed to fail along well-defined shear planes with inclinations of 63º and 57º (from horizontal), for the intact and reconstituted soil, respectively. The reconstituted samples show, together with the more gentle orientation, a thicker shear plane of approximately $11xd_{50}$, compared to the $7xd_{50}$ of the intact soil. Marked differences were observed between the mechanical behaviours of the intact and reconstituted samples, as shown in Figure 2. The intact soil showed a peak strength that is significantly higher than that of the reconstituted soil, and a correspondingly greater degree of strain-softening. The greater peak stress ratio, stiffness and rate of dilation exhibited by the intact material, when compared to the reconstituted soil, have been well documented (e.g. Cresswell and Powrie, 2004); the grain-scale phenomena underlying these behaviours, however, remain poorly understood.

In order to investigate the internal fabric of the soil and the mechanism of deformation at the grain-scale, the tests were stopped at different stages of loading and the samples were impregnated with resin while in the cell. A low viscosity resin was used to avoid soil disturbance. Details of the samples considered here are summarised in Table 1 for the initial stage prior to loading (Stage 0) and in Table 2 for the two post-peak load stages (Stages 3 and 4). The data on Table 1 include intact samples (sample reference 'Int') and reconstituted samples (sample reference 'Rec'). The axial strain (ε_a), the stress level (given by the ratio between deviator stress and mean stress, q/p') and the specific void ratio (υ) for the relevant loading stages are provided. The loss of the initial homogeneity of the samples following the formation of the shear band the fabric evolution outside and inside the shear band to be differentiated; samples are denoted 'including shear band' since the small thickness of the shear plane means that the samples are not likely to be exclusively within the shear band region.

3D imaging process

Small cores (5mm diameter) were extracted from regions containing the shear band and from the bulk of the impregnated triaxial samples. The cores were imaged using x-ray computed tomography (micro-CT) in the nanotom (phoenix|x-ray, GE). Micro-CT is a high resolution imaging technique that enables the internal structure of soil to be investigated (e.g. Oda et al., 2004). The 3D images obtained are maps of x-ray attenuation based on composition and density of the material. Therefore, each voxel (3D pixel) in the image has an intensity value, or colour, associated with the material it represents. The voxel size of the images was 5µm, i.e. approximately 0.015×d_{50}, where d_{50} is the median particle diameter. The images were segmented in order to identify the individual grains, each particle-phase voxel was assigned an integer identification number (p_i) to associate it to a specific grain. Contacts between two given particles were identified along the boundaries by considering the voxel p_i number. For two contacting particles, with intensity values p_1 and p_2, the particle p_1 voxels were classified as contact voxels if they connected to a voxel of value p_2, where $p_2 \neq p_1$ and $p_2 \neq 0$ (as the void space has intensity 0). The voxel contact classification used in this study was based on a 6-connectivity voxel neighbourhood relation, and required a total of six orthogonal 'passes' through the data along the x, y and z directions (Fonseca, 2011).

STATISTICAL ANALYSIS OF THE CONTACT VECTORS

The vectors considered for this analysis were the contact normal vector orientation (CNV) and the branch vector (BV), as illustrated in Figure 3. The vector defining the contact normal was obtained by applying a least squares regression to identify a best-fit plane for each surface defining the contact and this plane defined the contact normal orientation. The branch vector is defined as the vector connecting the centroids of two particles in contact. In the case of spheres BV and CNV are coincident, however in real sand the irregular shape of the grains imparts significant orientation differences.

Angular histograms analysis

A convenient away of visualising the orientation distribution of large datasets of vectors is to use planar rose diagrams. These angular histograms show the distribution of the orientations of the 3D vectors projected onto a specific plane; in the cases presented here the vertical plane was chosen and the angle was measured from the horizontal plane. The contact vectors have an orientation, but not a direction, the force at each contact will act equally on the two contacting particles, but in opposite directions, i.e. a vector with an angle of 30 º has the same orientation as a vector with an angle of 210 º; thus, only half of the plane is considered. An extra feature of rose diagrams is the possibility of shading each bin by a scalar parameter whose normal orientations lie within that bin, e.g. average area of the contacts, particle diameter or particle aspect ratio.

For the intact sample prior to loading, these vectors show a near isotropic distribution as illustrated in Figure 4a and 4b for the CNV and BV respectively with the shading indicating contact area in both cases. The slight bias along the horizontal and vertical directions is related to the use of a 6-connectitvity for the contact detection, which favours the normal directions to the voxel faces, in other words, the vertical and horizontal directions. It is likely that using a 16-connectivity in the contact detection phase would avoid this bias and should therefore be considered in future studies. For the reconstituted samples the distribution is less isotropic with a slight increase in the number of contact normal vectors oriented along the horizontal plane, as shown in Figures 4c and 4d. It is interesting to note that contacts with larger areas (darker bins) tend to have more horizontal orientations; this holds true for both CNV and BV for the reconstituted sample and for the CNV of the intact sample; this trend is not observed for the BV of the intact sample.

It is important to emphasise the differences in the nature of the contacts for the intact and reconstituted soil. Because of the locked nature of the intact soil, the contacts comprise extended surfaces formed though the geological history of the soil, with measured average areas as high as 450voxels (values shown in the colourbar), this is further discussed in Fonseca et al. (2013c). The contacts of the reconstituted material were formed during the tamping and vibration used to produce dense samples in the laboratory and the associated surface areas are significantly smaller than those observed in the intact samples with measured average values lower than 200voxels. The number of contacts is also greater for the intact samples as indicated by the number of vectors per bin in the angular histograms, i.e. approximately 2800 per bin when compared to the 1500 per bin for the reconstituted sample (note that different scales are used to provide better detail of the data). For the same sand there are more contact normal vectors than branch vectors since two grains in contact can have multiple contact surfaces which results from the irregular shape of the grains. This difference is more pronounced for the intact samples.

As shearing progresses there is a clear reorientation of the contact normal vectors towards the direction of the major principal stress. This trend was observed for both intact and reconstituted samples at load stages 3 and 4 outside the shear band and it is demonstrated here for sample Int3 in Figure 5a. The reorientation of these vectors along the vertical direction supports previous observations from photoelastic tests and DEM analyses on the formation of columns of grains creating chains of transmitted stress. This realignment is more obvious for the CNV; however there a subtle realignment of the BV is evident in Figure 5b. Both Figures 5a and 5b show that vertically oriented vectors are predominantly associated with larger contacts (darker bins), for both CNV and BV. Figure 5c shows that for the sample including the shear band the predominant direction of the contact normal, for the reconstituted sample, deviates from the vertical direction, which is in agreement with the rotation and bending of the buckling force chains within the shear band (e.g. Oda and Kazama, 1998; Iwashita and Oda (1998), and this bias is predominantly represented by the large area contacts. This deviation is in agreement with previous studies that showed the buckling of force chains inside the shear band. For this sample the branch vectors with large contact areas are also more vertically oriented, however these vectors do not represent the most dominant orientation (Figure 5d).

The samples containing the shear band at load stage 4 presented in Figure 6, show similar trends to those observed at load stage 3. The CNV distribution for the intact sample again shows a dominant vertical orientation and the effect of the buckling of force chains is reflected in the slight asymmetric distribution shown in Figure 6a. For the reconstituted sample, the distribution of the CNV vectors presented in Figure 6c exhibits a more marked bias; the contacts with larger surface areas tend to be orientated in the direction of the shear band, this is also observed for the intact sample (Figure 6a). The distributions of the branch vectors shown in Figures 6b and 6d exhibit a less clear bias in the realignment of the vectors but the influence of the buckling of force chains is reflected in the more asymmetric distribution when compared with the samples from outside the shear band as shown in Figures 4b, 4d and 5b. An important observation from the rose diagrams in Figure 6 is the marked difference in the orientation of the contact normal and branch vectors. This is because the BV for a given contact depends on the on the shape and relative position of the particles in contact rather than simply in the orientation of the contact itself. These observations provide evidence of the better suitability of contact normal data to describe the microscale changes when compared to the branch vector data when non-spherical particles are used.

Fabric tensor analysis

A second order fabric tensor was used to investigate the preferred orientation of the dataset of CNV and BV vectors and their associated intensity. Following Satake (1982), the tensor was calculated as:

$$\Phi_{ij} = \frac{1}{N}\sum_{k=1}^{N} n_i^k n_j^k \qquad (1)$$

where N = the total number of vectors in the system and n_i^k = the unit orientation vector along direction *i*.

Fabric tensors were calculated for the contact normals (Φ_{ij}^{CNV}) and for the branch vectors (Φ_{ij}^{BV}). The dominant orientation of the dataset was quantified by the angle β given by inclination of the major principal eigenvector relative to the horizontal plane. The anisotropy of the specimen at each load stage was quantified by considering the difference between the maximum and minimum eigenvalues of the fabric tensor, i.e. Φ_1- Φ_3. An isotropic system will have Φ_1- Φ_3=0 and an increase in the bias of the vector distribution will cause an increase in the anisotropy.

The results for the contact normal and branch vector data are presented in Table 3 together with the number of vectors used. The CNV data show much higher anisotropy values when compared to the BV which is in accordance with the stronger alignment of the vectors observed in the rose diagrams. This trend is slightly more pronounced for the samples outside the shear band. The evolution of the orientation parameter β^{CNV} is compared with the macro response given by the stress:strain curves of both the intact and reconstituted soil, Figure 7, for the CNV data. The samples outside the shear band, both intact and reconstituted, show β^{CNV} values greater than 80º, i.e. a deviation from the vertical of less than 10º. For the samples containing the shear band (data points marked with circles), β^{CNV} takes slightly lower values, between 60-80º. This is in agreement with what was observed in the rose diagrams in Figure 4. Similarly to the steady state reached by the deviatoric stress at stages 3 and 4, β^{CNV} appears to reach relatively stable values for the regions inside and outside the shear band, although the limited data prevents more conclusive observations on this. For the branch vector data, the distribution of the vectors is more isotropic with no clear dominant orientation, as shown by the rose diagrams, therefore, the physical meaning of β^{CNV} is less significant.

Contact normal and branch vector relationship

Typically DEM simulations use ideal circular or spherical particle geometries for which the contact vectors and the branch vectors are collinear. For real soils, however, they are unlikely to be collinear as the schematic in Figure 3 shows. In this study, the relationship between the contact normal and the branch vector orientations was investigated by considering the angle between the vectors, i.e. α as defined in Figure 3. To investigate the relationship between α and grain characteristics in terms of their morphology and the way they form contacts, the distribution of α is presented using rose diagrams shaded by elongation index (EI), the sphericity (S) and the contact area (CA). The elongation index (EI) is defined as:

$$EI = b/a \qquad (2)$$

where a = length of the major principal axis and b = length of the intermediate principal axis, obtained by applying Principal Component analysis to the cloud of voxels defining each individual grain, as described in Fonseca et al. (2012). The sphericity (S) was calculated by:

$$S = \frac{\sqrt[3]{36\pi V_p^{\,2}}}{SA} \qquad (3)$$

where V_p = particle volume; SA = surface area of the particle. Both EI and S take values between 0 and 1 and since each contact is formed by two grains the indices used here correspond to the grain with the larger volume. The contact area parameter is measured in voxels.

Figure 8 includes the α data obtained at loading stage 3, for the intact sample outside the shear band and the intact and reconstituted samples including the shear band. For all the samples the angle α varied between 0 and 60° with the most frequent value being about 20°. Referring to Figures 8a, 8d and 8g we can observe that as the geometry deviates from a regular shape, and the elongation index takes lower values (darker bins), α increases, i.e. elongated grains in contact are more likely to lead to a greater difference between the CNV and the BV vectors. The angle α is also sensitive to the sphericity of the contacting grains, as depicted in Figures 8b, 8e and 8h. For sphericity values closer to 1, i.e. grain shape close to a sphere, α takes values closer to 0 as would be expected. A clear trend is also found for the contact area (CA measured in voxels) with α increasing as the contact area decreases, Figures 8c, 8f and 8i. These observations suggest that grains with extended contact surfaces are more likely to show a better approximation between the orientation of the BV and the CNV vectors.

NETWORKS OF STRESS TRANSMITTING PARTICLES

Methodology

Networks of contacts and contact forces have received considerable attention in recent literature (e.g. Tordesillas et al., 2015; Hanley et al., 2014; Lin and Tordesillas, 2014; Ardanza-Trevijano et al. 2014; Newman, 2003). In the absence of force measurements, this study makes use of geometrical considerations to generate the strong network of stress transmitting particles. The information extracted from the tomographic data is used to construct the contact network. Similarly to the above studies, this contact network is represented by a collection of nodes and links, with nodes representing the grains and the connecting links representing contact between two grains.

As shown previously, in order to support the increasing axial load, particles tend to organise in columnar structures transmitting the stress along the direction of the major principal stress and this is better captured by the contact normal vector. Thus, we use the orientation of the contact normals and the graphical representation of the network is obtained by connecting the centroids of the grains in contact. The potential force chains and the associated grains are identified here using the following conditions:

1) *the stability criterion*: the grain participates in at least one 3-cycle contact triangle that provide lateral support to the chain and inhibiting rotations; this criterion infers stability.
2) *the load transmission criterion*: the contact normals forming each 3-cycle are approximately parallel to the major principal stress (near-to-vertical), in other words, the grain participates in a quasi-linear cluster of three or more grains.

Further details on each criterion are given below and this methodology was applied to the intact samples at load stage 3 both from outside and including the shear band, Int3 and Int3S, respectively.

1) Stability criterion

Following Tordesillas et al. (2010), 3-cycle clusters are clusters of three grains in mutual contact. These particles were filtered from the initial contact network using a MATLAB (Mathworks, 2013) script that identifies whether a given grain is in contact with other two other grains, which in turn also form a contact between them. Figure 9a shows a 2D schematic of the truss abstraction overlaid on a particle assembly; the nodes are at the particle centroids. Note that the analysis was done in 3D but for ease of visualisation, a 2D section is presented here. The 3-cycle contact triangle topologies identified for the entire sample form the truss network. Figure 9b shows a section through the 3D truss where only the grains forming at least one 3-cycle contact triangle are accounted for. For ease of visualization, the network is presented for a section with a thickness of 60 voxels corresponding to 300μm (approximately the soil median grain diameter). Figure 10 compares similar sections through the truss network for the sample outside the shear band (Figure 10a) and the sample containing the shear band (Figure 10b). It can be clearly seen that the effect of the shear band contributes to the exclusion of a larger number of grains which do not participate in any 3-cycle contact from the truss network. Table 4 summarizes the number of grains comprising each network. For sample Int3, outside the shear band 95% of the grains forming the contact network satisfy the stability criterion. For the sample including the shear band, the stability criterion is satisfied by 87% of the grains in the contact network. This reduction in the number of grains satisfying the criterion is assumed to be associated with the loss of stability of the columnar structures in the shear band.

2) Load transmission criterion

A second MATLAB script was developed to identify the grains satisfying the load transmission criterion. In a first pass, the code identifies from each of the 3 contacts composing the cycle, those for which the contact normal vector is near vertical. The acceptable deviation angle from the vertical direction was assumed to be 35° (in spherical coordinates) to account for a degree of curvature in the force chains. The identification numbers (p_i) of the grains forming the contacts that passed the near-to-vertical selection were stored and used to investigate whether they form a quasi-linear cluster of at least three grains. A given grain 'p_i' will satisfy this condition if it forms a contact with a grain 'p_j' and a grain 'p_k' located below and above the grain's centroid, respectively. As shown in Table 4, only 54% of the grains satisfy mutually the load transmission and stability criteria for the sample outside the shear band. For the sample including the shear band, this value is lower, i.e. only 39% of the grains originally forming the contact network form the force chains orientated in the direction of the major principal stress. The bending and rotation of the force chains within the shear band suggested in previous studies supports the markedly reduction in the number of vertical columns measured here for the sample containing the shear band.

Load-bearing particles forming the force chains

The grains that were identified to satisfy both the stability and the load transmission criteria are assumed to belong to a force chain. The methodology employed to obtain these load bearing grains is summarised in the flowchart presented in Figure 11. Figure 11a shows the 3D tomographic image acquired and post-processed as detailed in the '3D imaging process' Section. The outcomes of the image analysis procedure include the coordinates (x,y,z) of the grains' centroids and contact normal vectors of the grains in contact. This information was used to draw the contact network formed of lines connecting the centroids of the grains in contact, as displayed in Figure 11b for the entire sample. The truss network illustrated in Figure 11c is represented by segments connecting the centroid of only the grains in contact with at least two other grains, i.e. taking part in a 3-cycle triangle contact topology. Finally, the load bearing grains forming force chains are displayed in Figure 11d by lines joining centroids of contacting grains that are in truss network where the contacts meet the load stability criterion. Note the significant difference between the initial contact network formed by 2574 grains and the load bearing network formed by 1392 grains for the sample outside the shear band as shown in Table 4. For the sample including the shear band, only 754 grains out of 1912 initially forming the contact network, are found to compose the force chains. This is an expected result since the stable and quasi-vertical columnar structures of grains tend to decrease in number as deformation inside the shear band progresses.

Quantitative description of the load-bearing particles

Particles in the force chains are primary load bearers that take an active role in the transmission of stress. While the particle-scale mechanisms of stress transmission underpin the macro-response of the material, the characteristics of the grains forming the force chains and the nature of their contact topologies remain largely unknown.

The orientation of a particle can be described by the orientation of its major axis (Fonseca et al., 2013b; Paniagua et al, 2015). Fonseca et al. (2013b) considered the same triaxial samples investigated here and showed that for the intact material the grains are preferentially orientated in their most stable position, that is, their minor principal axes are approximately vertical. Triaxial compression causes a readjustment of the orientations; as the load increases the material dilates and causes grain breakage along the initial existing fissures. Since the newly-detached grains are randomly oriented, the result is an approximately isotropic distribution as presented in the rose diagram of the particle's major axis depicted in Figure 12a. When only the grains forming the force chains are used, the rose plot exhibits a higher concentration along the horizontal plane which indicates that the bearing grains tend be in stable positions (Figure 12b). The angular histogram of the grains forming the truss network does not show significant differences when compared with the contact network (shown in Figure 12a) and therefore is not presented. For the sample containing the shear band, the distribution is affected by the appearance of the shear band and so interpretation is less straightforward, as discussed in Fonseca et al. (2013b); however there is a more pronounced bias towards near-horizontal directions for particles in the force chains (Figure 13b) when compared with the contact network as a whole (Figure 13a). For both Figures 12 and 13 no clear correlation can be found between particle orientation and particle elongation ratio (Equation 2), the latter given by the shading of the bins. The particle size distribution, given by the length of the intermediate axis of the grains, for the three networks is presented in Figure 14. These data suggest that force chains tend to be formed by the larger grains and this trend is more pronounced for the sample containing the shear band (Figure 14b) when compared to the data from outside shear band (Figure 14a). Previous numerical studies also reported that strong force chains pass preferentially through larger grains with a significant number of small grains being excluded from the force network (Voivret et al., 2009).

The coordination number (CN) distribution presented in Figure 15 shows that through the selection process to isolate those grains forming the force chains, the CN value tends to increase, which suggests that the load bearing grains have higher number of contacts. The median CN values for each network are provided to guide the comparison. The difference in CN between truss network and the force chains is greater for the sample including the shear band when compared to the grains outside the shear band, as can be observed when comparing Figures 15a and 15b. The plot of CN against the number of triangular trusses formed in both the truss and the force chain networks presented in Figure 16 suggests that although higher CN values are associated with grains forming large number of trusses, high CN values alone may not be suitable indicator of stability. There are particles with CNs as high as 8 that do not participate in any truss structure. Particles forming force chains tend to have CN values between 4 and 16.

The evolution of the contact surface area for the three networks is presented in Figures 17a and 17b for the samples outside the shear band and containing the shear band, respectively. Similarly with the trend observed for the particle diameter and CN, a shift of the curves towards larger contact areas from the contact network to the force chains, is observed here. Despite the small evolution the trend is consistent and is in agreement with the realignment of the contacts with larger surfaces observed shown in Figures 5 and 6.

Spatial distribution of the force chains

Figure 18a shows the spatial distribution of the chains through a selected section of 60 voxels thickness. Although the force chains were identified for a minimum of 3 particles in a quasi-linear form, these chains are connected additional force chains as can be seen by expanding in the three dimensional space to a thickness of 300 voxels in Figure 18b. Three-dimensional visualization of the spatial distribution of force chains is not trivial, however it can be observed that there are some gaps in the network. As suggested in Ghedia and O'Sullivan (2012), it is believed that in the gap between two dominant force chains there is a network of weaker force chains transmitting smaller contact forces, which contribute to stabilise the strong force chains.

A methodology based on image processing tools to enable visualisation of the spatial distribution of the force chains is used following Fonseca et al. (2014). Here, this previous work was improved by considering the contact normal vectors in lieu of the branch vectors. The method uses as starting point the truss network so that the stability criterion is satisfied. The second condition is to select only the near-to-vertical contact normal vectors, i.e., using an angle of 35° (in spherical coordinates) to satisfy the load transmission criterion as described previously. The vectors that satisfy both conditions, were allocated into a 3D space of the same dimension as the original image of the sample (i.e., 600 voxels cube) which we call the vectorial volume (VV). While the orientation and the contact surface areas correspond to the contact normal the vectors are displayed by connecting the centroids of the grains in contact. Figure 19a shows the maximum intensity projections of the VV (calculated for a volume of 50 voxels thickness). The colour of the line joining the particle centroids indicates the contact area (larger contacts are represented by a brighter colour). These projections were filtered using a low pass filter (Reyes-Aldasoro, 2015) in order to enhance the selection of the contacts with a greater intensity (brighter colour) that are, therefore, more likely to belong to the main network of contacts, shown in Figure 19b. This was followed by the application of a watershed transform (Reyes-Aldasoro, 2015) to discard shorter and unconnected lines. The resulting network of the stress transmitting grains is shown in Figure 19c for the sample Int3 (outside the shear band). The same procedure was applied to the data for sample Int3S, including the shear band, is illustrated in Figures 20a, 20b and 20c. We hypothesise that these quasi-vertical columnar structures are closely correlated to the networks of stress transmitting particles. The distribution of the force chains was quantified by measuring the density value of the columns. The values measured for a planar section of 60^2 voxels (approximately d_{50} length) were of 1.2 for the sample outside and 0.4 for the sample containing the shear band. The lower value of 0.4 can be seen as an indication of the buckling of the columnar structures caused by the movement of the shear band and the consequent decrease in the number of near vertical force chains.

CONCLUSIONS

Micro-CT data on specimens of sand enables the investigation of the stress transmission phenomena that accounts for the effect of the grain morphology and contact topology. The observed realignment of the contact normals in the direction of the major principal stress is seen to be linked to the formation of contacts with larger surface area. The effect of the shear band formation and the associated bending or buckling of these columns has been demonstrated by a greater deviation of the predominant direction of the contact normal vectors from the vertical plane. These observations hold true for both intact and reconstituted samples. The two parameters extracted from the fabric tensor of the contact normal vectors, the anisotropy and major eigenvector, were shown to be able to quantitatively describe the subsequent changes in the topology of the stress transmission mechanisms during triaxial compression. The near-vertical realignment of the branch vectors in the post-peak regime and the bending in the shear plane were however less obvious. The difference between contact normal and branch vector was found to increase with the deviation from the spherical shape and with the decrease of the contact surface. Using the conditions of quasi-vertical contact normal vectors and 3-cycle contact, have enabled the identification and quantitative characterisation of the load bearing grains. It is suggested here that these grains tend to be oriented in most stable positions, with the major axis along the horizontal plane, and have on average higher number of contacts. The contribution of the larger surface contacts to the stability of columnar structures of grains was taken into account to develop a method able to provide the spatial distribution of the vectors defining the force chains. The kinematics of shear band formation caused a decrease in the number of the near vertical columnar structures when compared to material outside the shear band, which confirms earlier 2D physical and numerical model observation of force chain orientations in shear bands. This study presents new understanding on the primary fabric of stress transmitting particles and highlights the effect on the kinematical phenomena of the rich topology found in real sand.

ACKNOWLEDGEMENTS

The first author would like to acknowledge the financial support from the Portuguese Government Body, Fundação para a Ciência e a Tecnologia (FCT) and from City University London. The authors are also grateful to GE Measurement & Control Solutions (Germany) for their support in the micro-CT image acquisition.

REFERENCES

Ardanza-Trevijano, S., Zuriguel, I., Arévalo, R., Maza, D., 2014. Topological analysis of tapped granular media using persistent homology, *Physical Review E* 89, 052212.

Barreto D, O'Sullivan C., 2012, The influence of inter-particle friction and the intermediate stress ratio on soil response under generalised stress conditions, Granular Matter, Vol: 14, Pages: 505-521, ISSN: 1434-5021.

Bouchaud, J. P., Claudin, P., Levine, D., Otto, M., 2001. Force chain splitting in granular materials: A mechanism for large-scale pseudo-elastic behaviour. The European Physical Journal E, 4(4), 451-457

Cresswell, A., Powrie, W., 2004. Triaxial tests on an unbonded locked sand. *Géotechnique* 54 (2), 107–115

Dusseault, M. B., Morgensten, N.R. Locked sands, 1979. Q. J. Engng Geol. 12, 117-131

Fonseca, J., O’Sullivan, C., Coop, M., Lee, P.D., 2012. Non-invasive characterization of particle morphology of natural sands. *Soils and Foundations* 52(4), 712-722.

Fonseca, J., Bésuelle, P., Viggiani, G., 2013a. Micromechanisms of inelastic deformation in sandstones: an insight using x-ray micro-tomography. *Géotechnique Letters* 3(2), 78–8.

Fonseca, J., O’Sullivan, C., Coop, M., Lee, P.D., 2013b. Quantifying evolution soil fabric during shearing using directional parameters. *Géotechnique* 63(6), 487-499.

Fonseca, J., O’Sullivan, C., Coop, M., Lee, P.D., 2013c. Quantifying evolution soil fabric during shearing using scalar parameters. *Géotechnique* 63(10), 818-829

Fonseca, J., 2011. The evolution of morphology and fabric of a sand during shearing, PhD Thesis, Imperial College London

Fonseca, J., Reyes-Aldasoro, C.C., O’Sullivan, C., Coop, M.R., 2014. Experimental investigation into the primary fabric of stress transmitting particles, Geomechanics from Micro to Macro, CRS Press, 1019-1024.

Gao, Z., Zhao, J., Li, X.-S., Dafalias, Y. F., 2014 A critical state sand plasticity model accounting for fabric evolution. *Int. J. for Num. and Anal. Meths in Geomechanics*, 38 (4), 370-3.

Hanley, K.J., Huang, X., O’Sullivan, C., Kwok, F.C., 2014. Temporal variation of contact networks in granular materials, *Granular Matter*, 16, 41-54.

Hanley KJ, O'Sullivan C, Wadee MA, Huang X., 2015. Use of elastic stability analysis to explain the stress-dependent nature of soil strength. R Soc Open Sci 2(4):150038.

Hasan, A., Alshibli, K.A., 2010. Experimental assessment of 3D particle-to-particle interaction within sheared sand using synchrotron microtomography. *Géotechnique* 60(5), 369-379.

Iwashita, K., Oda, M., 1998. Rolling resistance at contacts in simulation of shear band development by DEM. Journal of engineering mechanics, 124(3), 285-292.

Kumanr, N., Luding, S., Magnanimo, V., 2014. Macroscopic model with anisotropy based on micro-macro information *Acta Mechanica* 225, 2319-2343.

Lin, Q., Tordesillas, A., 2014. Towards an optimization theory for deforming dense granular materials, *Journal of Industrial and Management Optimization*, 10, 337-362.

Majmudar, T.S., Behringer, R.P., 2005. Contact force measurements and stress-induced anisotropy in granular materials, *Nature*, 435, 1079-1082.

Makse, H. A., Johnson, D. L., 2000. Schwartz, L. M. Packing of compressible granular materials. Physical review letters, 84(18), 4160.

Newman, M.E.J., 2003. The structure and function of complex networks. SIAM Rev. 45, 167.

Oda, M., 1972. Initial fabrics and their relations to mechanical properties of granular material. Soils and foundations, 12(1), 17-36.

Oda, M., Kazama, H., 1998. Microstructure of shear bands and its relation to the mechanisms of dilatancy and failure of dense granular soils *Géotechnique* 48(4), 465-481.

Oda, M., Takemura, T., Takahashi, M., 2004. Microstructure in shear band observed by microfocus X-ray computed tomography. *Géotechnique* 54(8), 539-542.

Ostojic, S., Somfai, E., Nienhuis, B., 2006. Scale invariance and universality of force networks in static granular matter. Nature 439(7078), 828–830.

Paniagua, P., Fonseca, J., Gylland, A.S., Nordal, S., 2015. Microstructural study of the deformation zones during cone penetration in silt at variable penetration rates, *Canadian Geotechnical Journal,* 10.1139/cgj-2014-0498.

Peters, J. F., Muthuswamy, M., Wibowo, J., Tordesillas. A. Characterization of force chains in granular material, *Physical Review E* 72, 041307, 2005

Radjai, F., Wolf, D. E., Jean, M., Moreau, J. J., 1998. Bimodal character of stress transmission in granular packings. Physical review letters, 80(1), 61.

Rechenmacher, A., Abedi, S., Chupin, O., 2010. Evolution of force chains in shear bands in sands. Geotechnique, 60(5), 343-351.

Reyes-Aldasoro, C.C., 2015. *Biomedical Image Analysis Recipes in MATLAB: For Life Scientists and Engineers*, Wiley-Blackwell, London.

Satake, M., 1982. Fabric tensor in granular materials. In IUTAM Conference on Deformation and Failure of Granular Materials.

Silbert, L.E., Grest, G.S., Landry, J.W., 2002. Statistics of the contact network in frictional and frictionless granular packings. Phys. Rev. E 66(6), 061,303.

Thornton, C., 1993. On the relationship between the modulus of particulate media and the surface energy of the constituent particles *J. Phys. D: Appl. Phys.* 26 1587.

Tordesillas, A, Muthuswamy, M., 2009. On the modelling of confined buckling of force chains *J. Mechanics Physics Solids* 57, 706–727.

Tordesillas, A., Walker, D. M., Lin, Q., 2010. Force cycles and force chains. *Physical Review E,* 81(1), 011302.

Tordesillas, A., Sibille, L., Pucilowski, S., Nicot, F., Darve, F., 2011. Microstructural evolution in diffuse granular failure: force chains and contact cycles. In Second International Symposium on Computational Geomechanics (ComGeo II).

Tordesillas, A., Tobin, S.T., Cil, M., Alshibli, K., Behringer, R.P., 2015 Network flow model of force transmission in unbonded and bonded granular media, Physical Review E.

Voivret, C., Radjai, F., Delenne, J. Y., El Youssoufi, M. S., 2009. Multiscale force networks in highly polydisperse granular media. Physical review letters, 102(17), 178001.

Zuriguel, I., Mullin, T., Rotter, J.M., 2007. Effect of particle shape on the stress dip under a sandpile. Phys. Rev. Lett. 98(2), 028001.

Table 1: Specific volume (v) of the intact and reconstituted samples prior to loading

Sample ref.	***v***	**Obs.**
Int0	1.48	Intact sample prior to loading
Rec0	1.50	Reconstituted sample prior to loading

Table 2: Summary of the intact and reconstituted samples investigated in the post-peak regime (ε_a=axial strain, q/p'=deviator stress/mean stress, υ=specific volume)

Sample ref.	**Load stage details**			**Sample location**
	ε_a (%)	***q/p'***	***v***	
Int3	3.89	1.73	1.63	Outside shear band
Int3S	3.89	1.73	1.63	Including shear band
Int4	7.94	1.38	1.67	Outside shear band
Int4S	7.94	1.38	1.67	Including shear band
Rec3	9.66	1.46	1.87	Outside shear band
Rec3S	9.66	1.46	1.87	Including shear band
Rec4S	12.35	1.46	1.70	Including shear band

Table 3: Results on the fabric tensor data for the contact normal (CNV) and branch vector (BV)

Sample ref.	**No. vectors**	**Fabric tensor parameters**			
		$(\Phi_1 - \Phi_3)^{CNV}$	β^{CNV}	$(\Phi_1 - \Phi_3)^{BV}$	β^{BV}
Int3	20096	0.088	82	0.061	84
Int3S	12906	0.142	72	0.027	64
Int4	12200	0.081	89	0.052	87
Int4S	24192	0.102	75	0.028	14
Rec3	19674	0.125	86	0.034	23
Rec3S	18924	0.143	76	0.022	63
Rec4S	17630	0.095	68	0.030	21

Table 4: Number particles in the different networks with the correspondent percentage of grains satisfying the stability criterion from contact to truss network and the stability plus load transission criteria from contact network to force chains

Sample ref.	Contact network	Truss network	Force chains
Int3	2574	2439 (≈95% Cont. Net.)	1392 (≈54% Cont. Net.)
Int3S	1912	1666 (≈87% Cont. Net.)	754 (≈39% Cont. Net.)

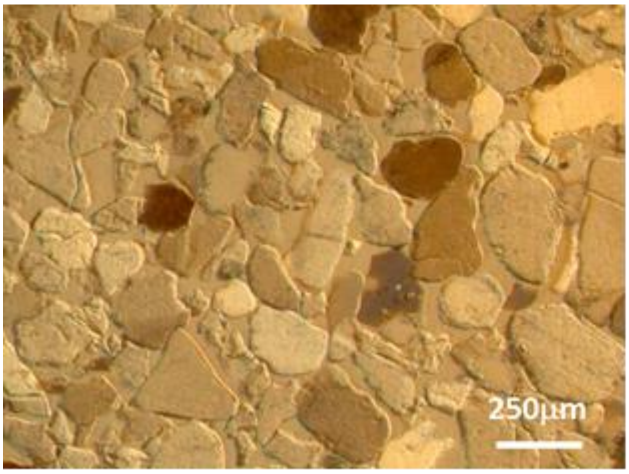

Figure 1. Microscope image of a thin section of Reigate sand under polarised light

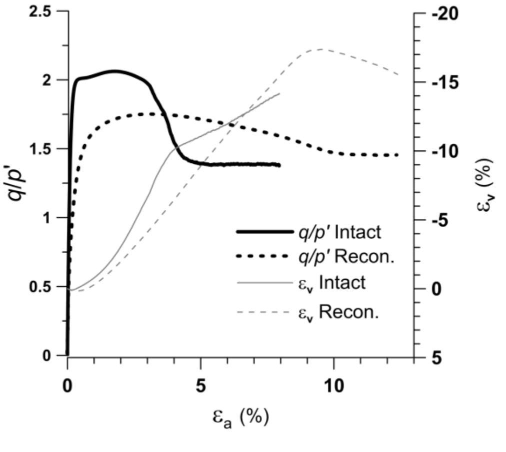

Figure 2. Mechanical and volumetric response for the intact and reconstituted samples

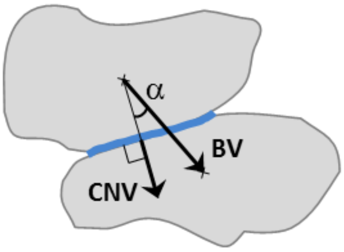

Figure 3. Schematic diagram illustrating the contact normal (CNV) and branch vector (BV)

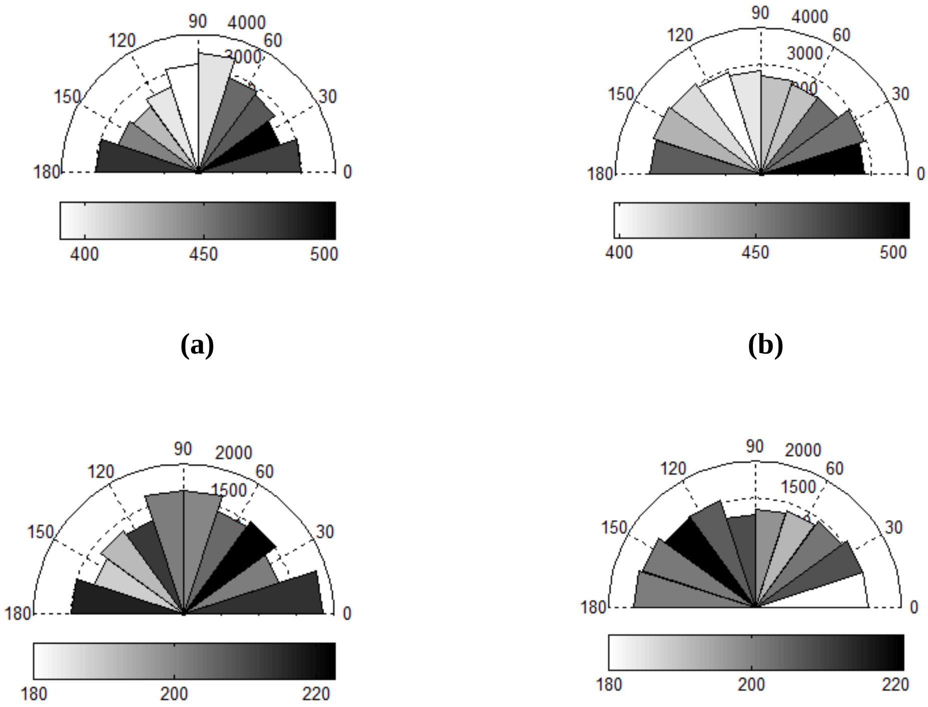

(a) (b)

(c) (d)

Figure 4. Rose diagrams for the intact and reconstituted specimens prior to loading (shading indicates average contact area in voxels); (a) CNV Int0; (b) BV Int0; (c) CNV Rec0; (d) BV Rec0

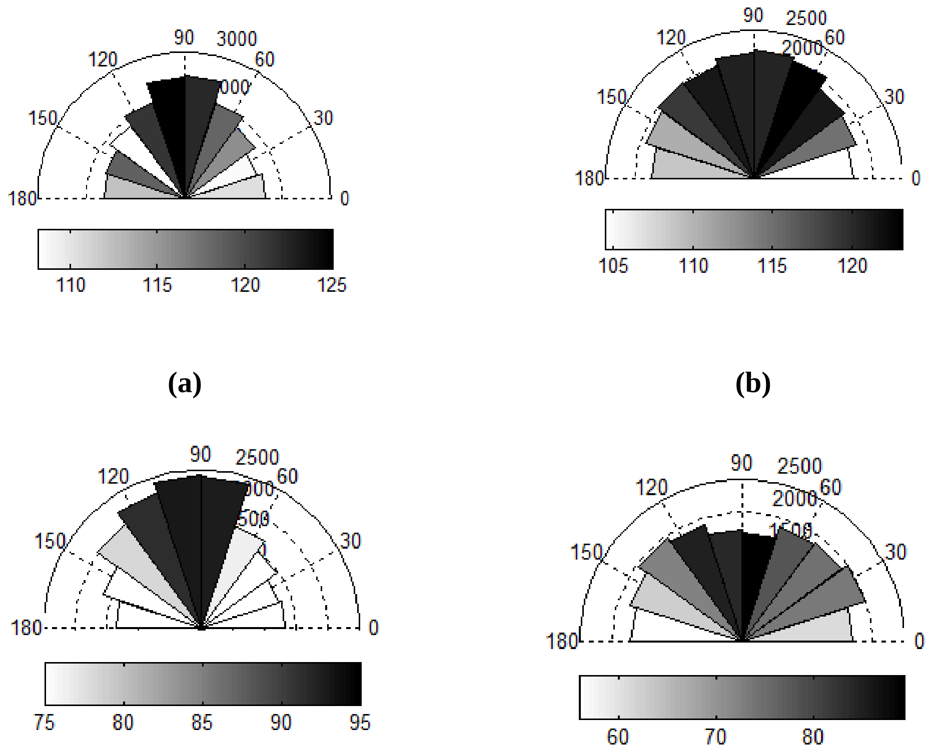

(a) (b)

(c) (d)

Figure 5. Rose diagrams for the specimens at load stage 3 (shading indicates average contact area in μm^2); (a) CNV Int3; (b) BV Int3; (c) CNV Rec3S; (d) BV Rec3S

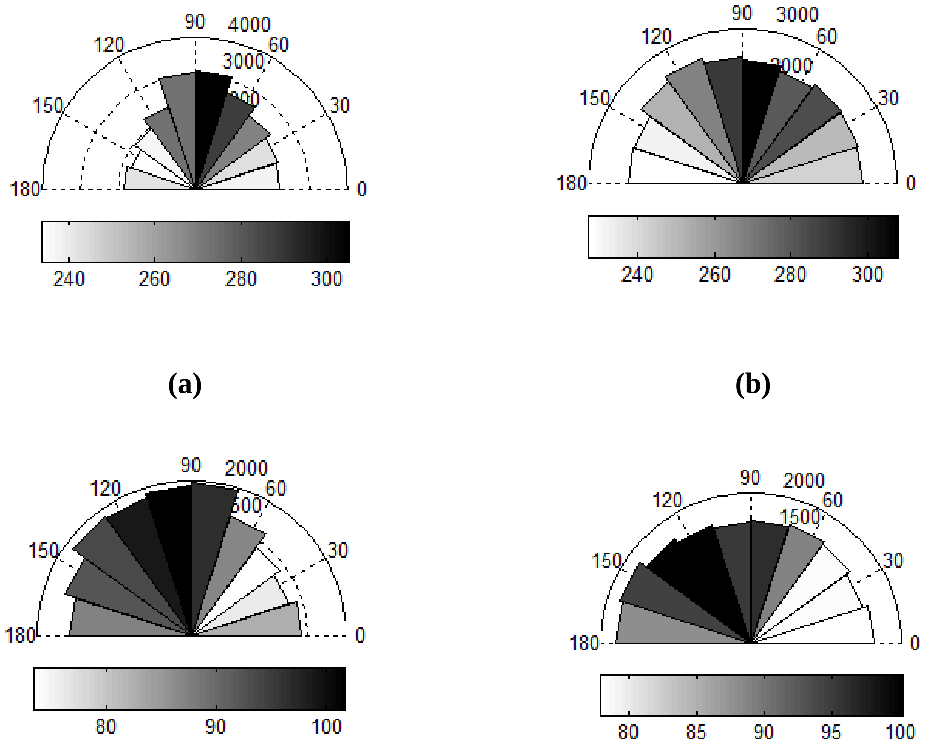

(a) (b)

(c) (d)

Figure 6. Rose diagrams for the specimens at load stage 4 (shading indicates average contact area in μm^2); (a) CNV Int4S; (b) BV Int4S; (c) CNV Rec4S; (d) BV Rec4S

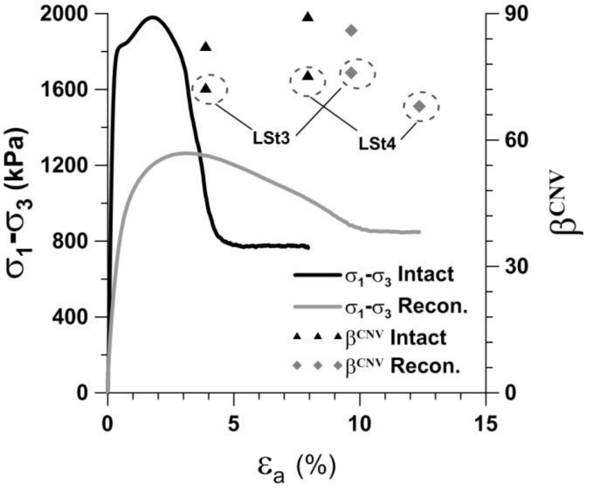

Figure 7. Evolution of the major principal fabric orientation for contact normal for load stages (LSt) 3 and 4, the data for the samples containing the shear band are marked with circles.

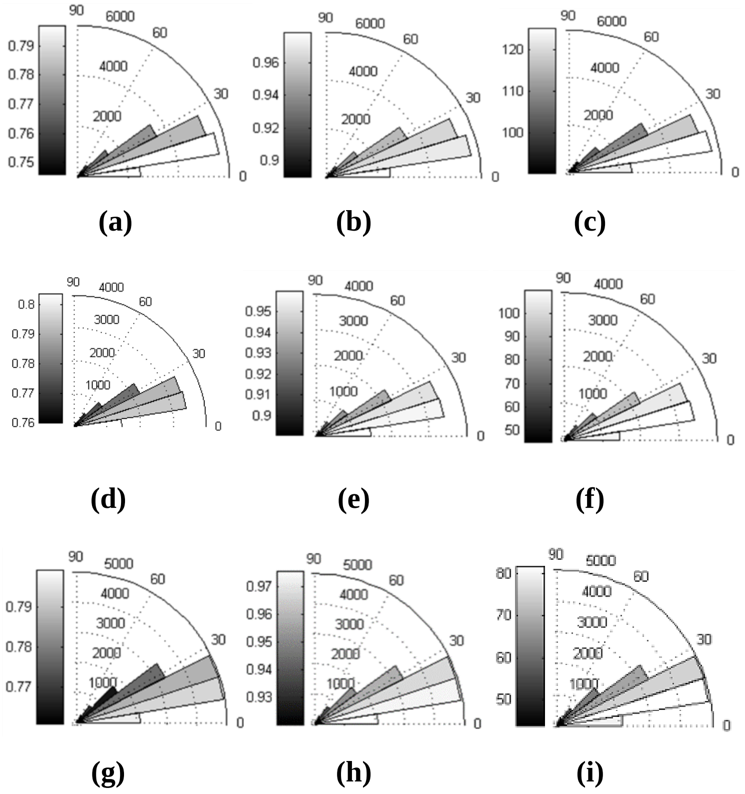

Figure 8. Distribution of angle α for the specimens: (a) Int3 shaded by EI; (b) Int3 shaded by S (c) Int3 shaded by CA; (d) Int3S shaded by EI; (e) Int3S shaded by S (f) Int3S shaded by CA; (g) Rec3 shaded by EI; (h) Rec3 shaded by S (i) Rec3 shaded by CA

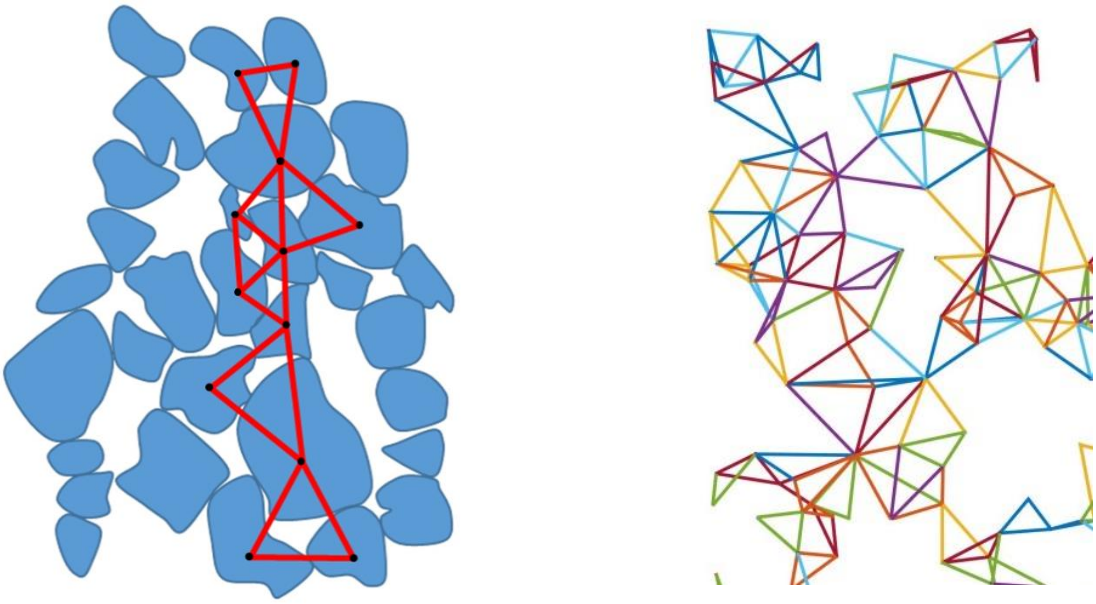

(a) (b)

Figure 9: a) Schematic of the truss network in a granular assembly, b) detail of a truss network for sample Iant3 for a section of 60 voxels thickness

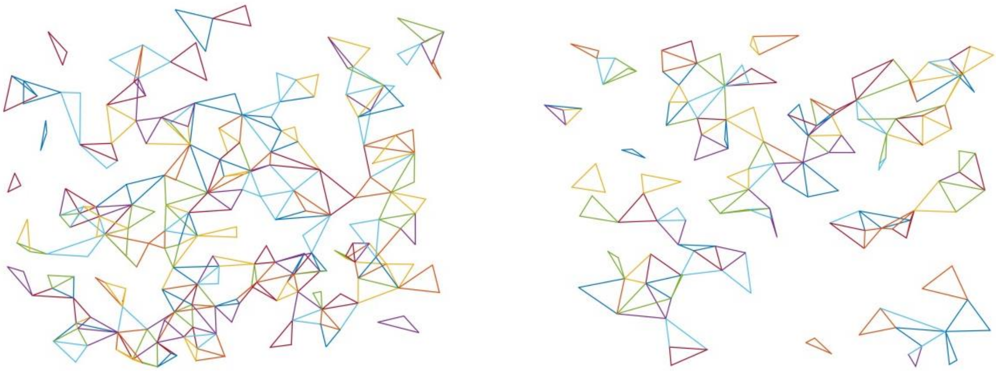

(a) (b)

Figure 10: Truss-like elements in a sub-volume (size in voxels: 600x600x60) for sample a) Int3 outside the shear band, b) Int3S, containing the shear band

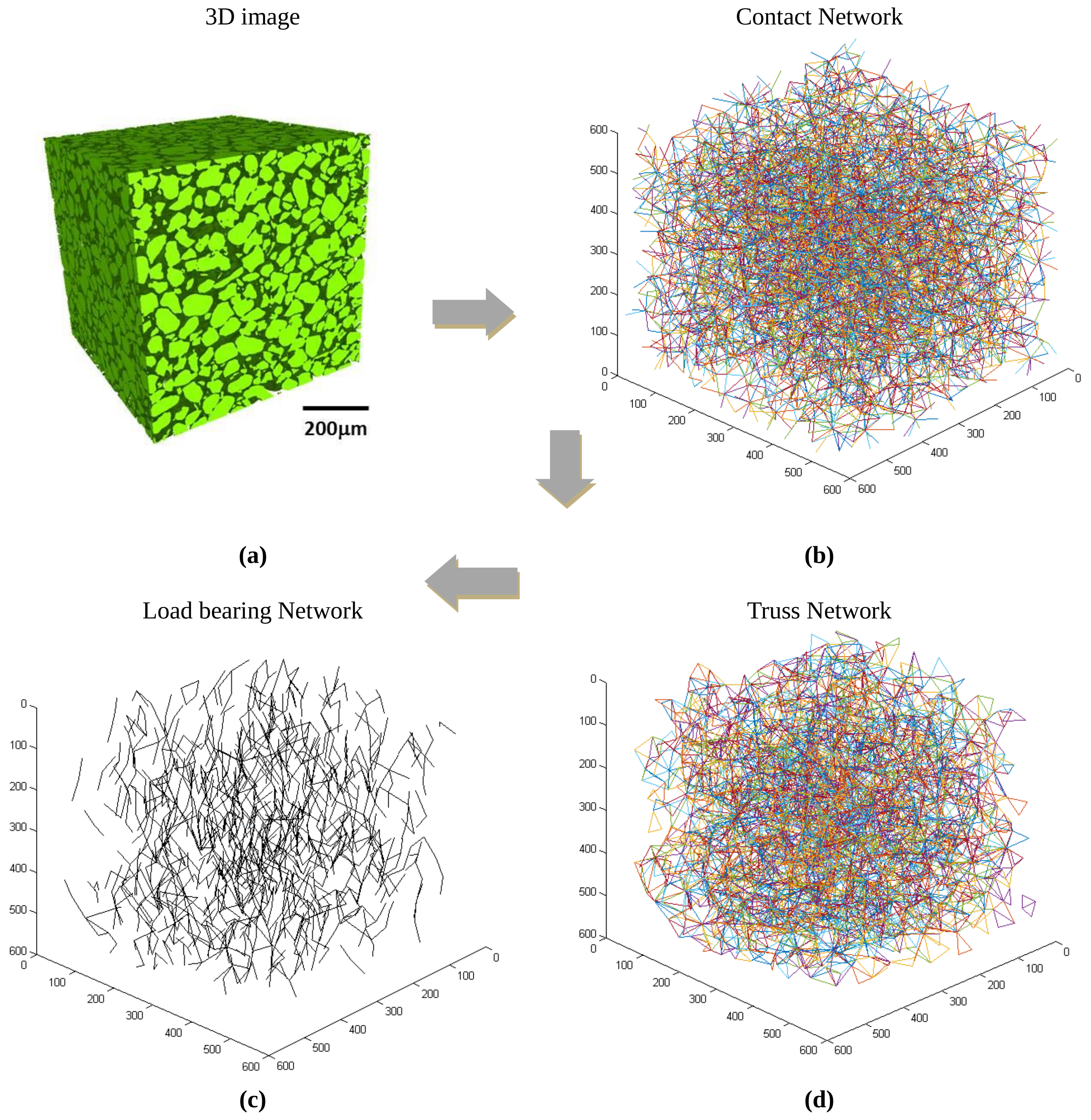

Figure 11: Methodology flowchart: (a) micro-CT image (600x600x600 voxels), (b) contact network, (c) truss network, (d) network of the stress transmitting grains or force chains (represented by segments connecting the centroids of the load-bearing grains)

(a) (b)

Figure 12: Rose diagrams showing the distribution of the particle orientation, given by the orientation of the particle's major axis, for the sample Int3 -shading indicates average elongation ratios of the particles within each angular bean: a) for the particles forming the contact network, (b) for the particles forming the force chains

(a) (b)

Figure 13: Rose diagrams showing the distribution of the particle orientation for the sample Int3S -shading indicates average elongation ratios of the particles within each angular bean: a) for the particles forming the contact network, (b) for the particles forming the force chains

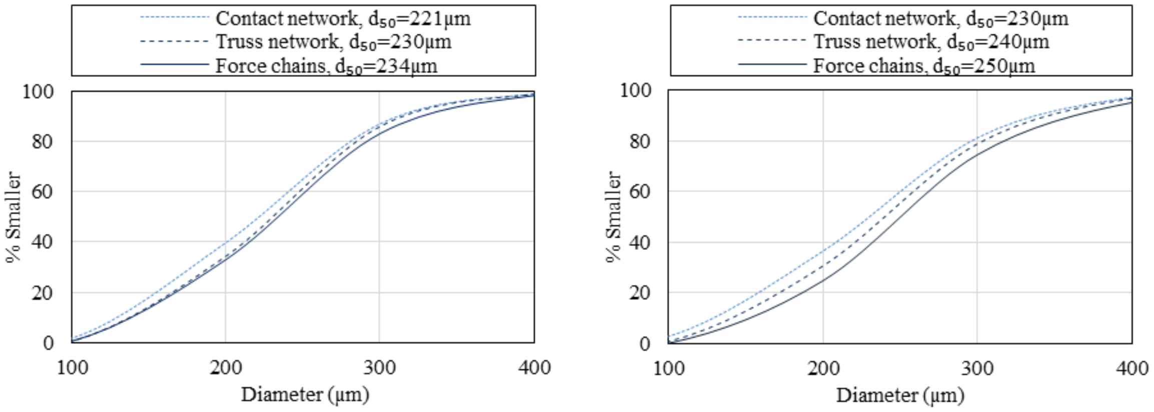

(a) (b)

Figure 14: Comparison of the particle size distribution for the grains composing each of the three networks, respectively: a) for sample Int3 outside the shear band and b) for the sample Int3S containing the shear band

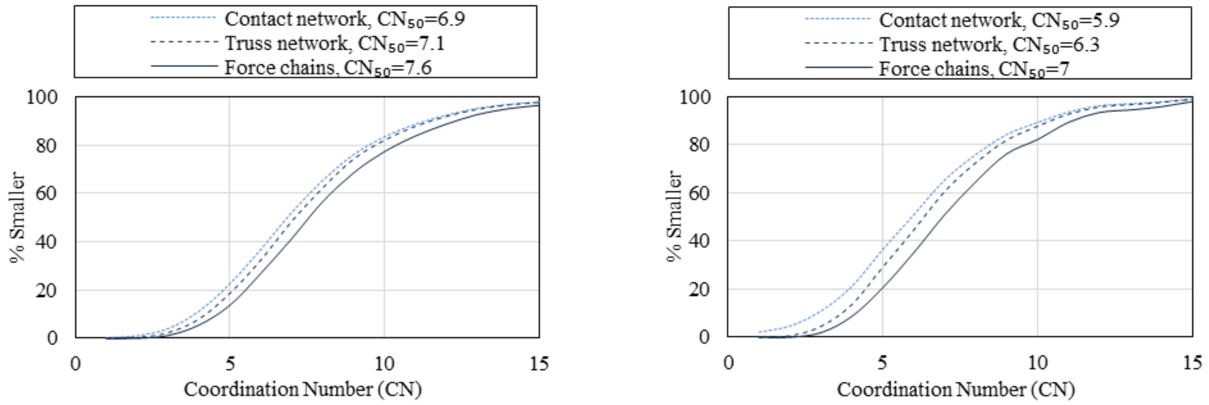

(a) **(b)**

Figure 15: Coordination number distribution for the grains composing each of the three networks, respectively: a) for sample Int3 and b) for the sample Int3S

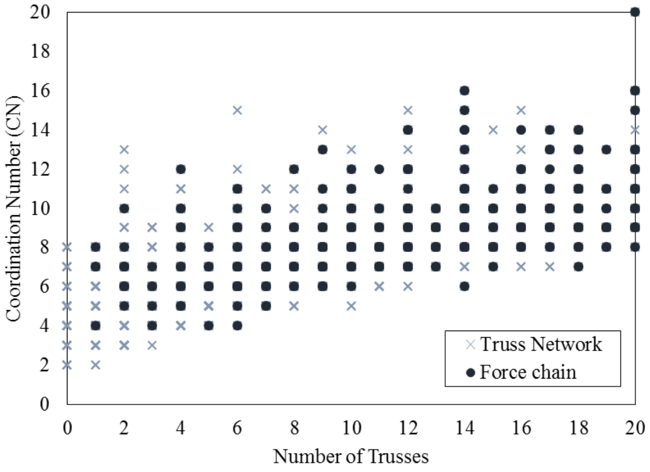

Figure 16: Coordination number versus number of trusses for both the truss network and the force chain for sample Int3

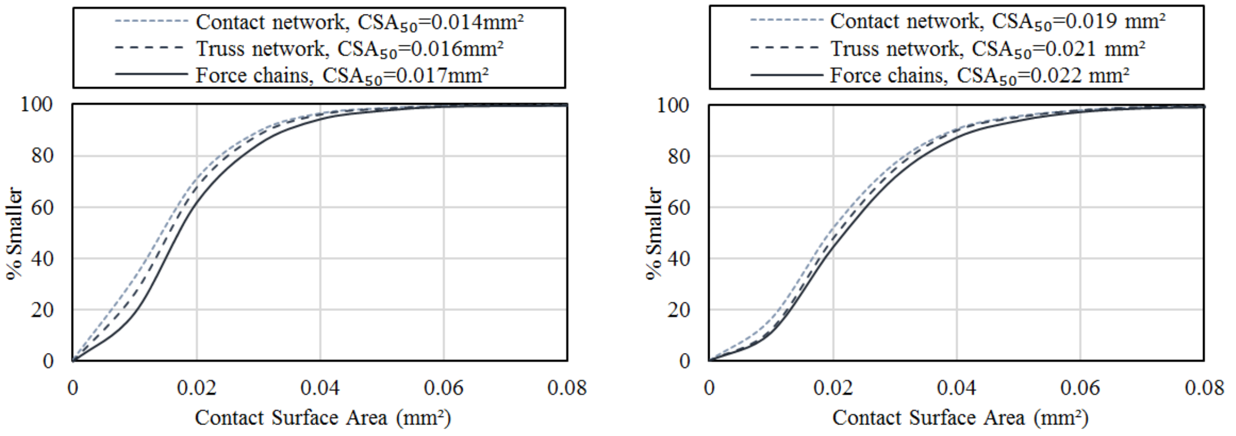

(a) **(b)**

Figure 17: Contact surface area distribution using all grains in the sample, using the grains that passed the stability criterion and the one that satisfy the load transmission criterion, a) for the intact sample outside the shear band and b) for the intact sample containing the shear band

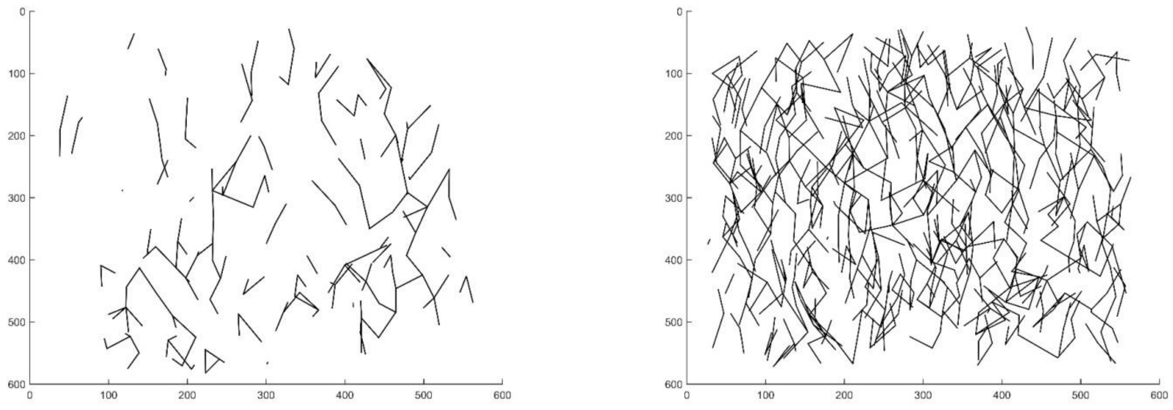

(a) **(b)**

Figure 18: Force chains obtained for sample Int3 for a section of: a) 60 voxels thickness and b) 300 voxels thickness

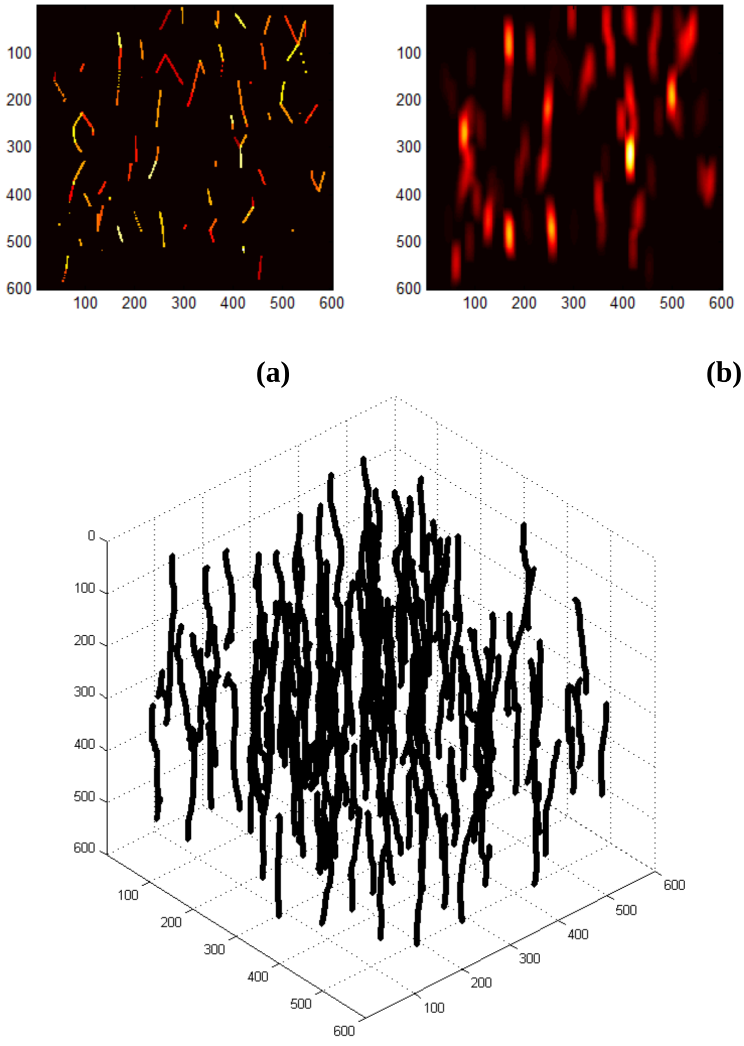

(a) (b)

(c)

Figure 19: Illustration of the steps to obtain the network of the stress transmitting grains for the sample Int3: a) 3D vectors, represented by the segments connecting the centroids of the grains forming quasi-vertical contact normals, the vectors associated with larger contact surfaces have brighter colours (only a projection is presented), b) 3D vectors following the low pass filter (c) final network

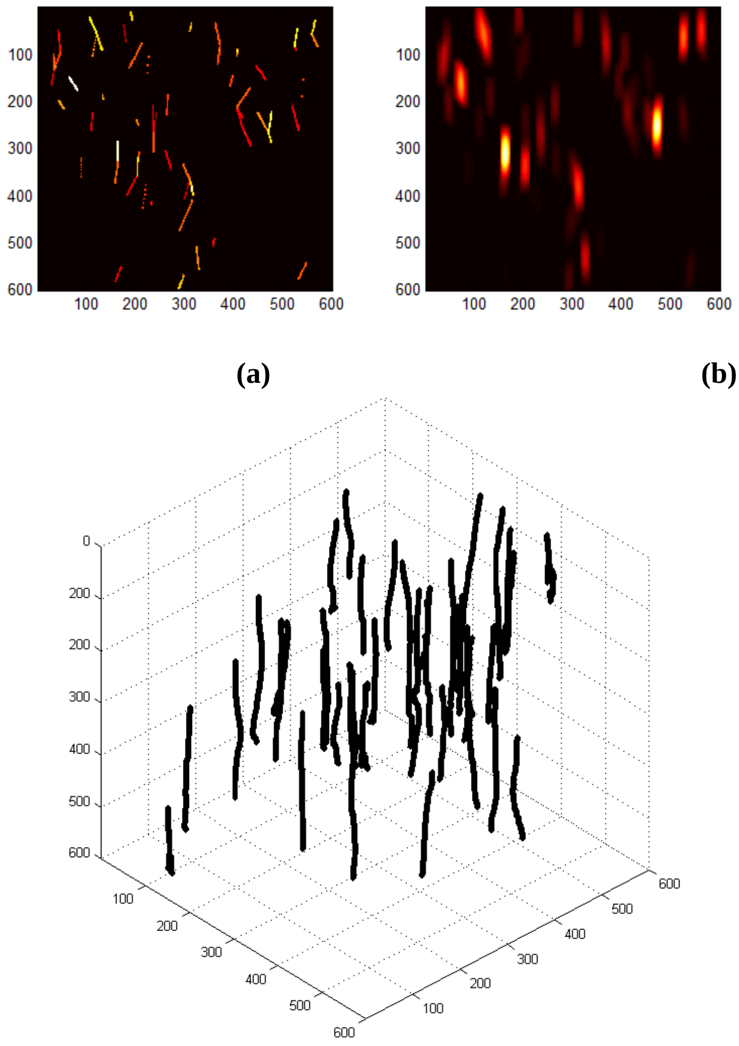

(a) **(b)**

(c)

Figure 20: Illustration of the steps to obtain the network of the stress transmitting grains for the sample Int3S: a) 3D vectors, represented by the segments connecting the centroids of the grains forming quasi-vertical contact normals, the vectors associated with larger contact surfaces have brighter colours (only a projection is presented), b) 3D vectors following the low pass filter (c) final network